Sensorless Back EMF Based Control of Synchronous PM and Reluctance Motor Drives—A Review

Zhendong Zhang, *Member, IEEE*

***Abstract*—This article reviews the state-of-the-art back electromotive force (EMF) based sensorless schemes for synchronous machines. Field-oriented control (FOC) of a synchronous machine requires real-time rotor position for decoupled torque and flux control. Extraction of rotor position without a sensor or sensorless control has been an enabling technology for the past few decades. Sensorless control using back EMF voltage induced by rotor movement is the most widely used method. However, the connections and differences between different methods have not been thoroughly investigated and documented. This article first reviews basic sensorless methods. The two implementation forms of an observer are examined to facilitate analysis. A detailed analysis puts in evidence the connections behind different methods in both stationary and synchronous reference frames. A summary is drawn that is meant to offer a few key points regarding different sensorless methods. Finally, a conclusion is given to summarize the major contributions of this article.**

***Index Terms*—Observers, permanent magnet machines, sensorless control.**

NOMENCLATURE

T_L	Load torque applied on the motor shaft.
T_e	Electromagnetic torque developed on the motor shaft.
R_s	Motor stator winding resistance.
L_{dq}	Motor stator winding inductance in *dq* axes.
L_d	*d*-axis stator self-inductance.
L_q	*q*-axis stator self-inductance.
L_0	$(L_d + L_q)/2$.
L_1	$(L_d - L_q)/2$.
λ_m	Permanent magnet flux linkage.
J_m	Rotor moment of inertia.
ω	Rotor actual angular speed.
ω_r	Rotor detected angular speed.
$\hat{\omega}$	Rotor estimated angular speed.
θ	Rotor actual angular position.
θ_e	Rotor detected angular position.
$\hat{\theta}$	Rotor estimated angular position.
p	Derivative operator.
3s/2r	Combined iPark and iClark transformation.
2r/3s	Combined Park and Clark transformation.
v_{abc}, i_{abc}	Motor three phase input voltages and output currents.
v_{dq}, i_{dq}	*dq* axes voltages and currents for motor modeling.
v_d, v_q	Stator voltage in dq synchronous reference frame.
i_d, i_q	Stator current in dq synchronous reference frame.
v_α, v_β	Stator voltage in dq stationary reference frame.
i_α, i_β	Stator current in dq stationary reference frame.

Manuscript received July 1, 2021; revised January 22, 2022; accepted March 12, 2022. Date of publication March 29, 2022; date of current version May 23, 2022. Recommended for publication by Associate Editor E. Armando.

The author is with Rockwell Automation, Mequon, WI 53092 USA (e-mail: zhdzhang@gmail.com).

Color versions of one or more figures in this article are available at https://doi.org/10.1109/TPEL.2022.3162963.

Digital Object Identifier 10.1109/TPEL.2022.3162963

I. INTRODUCTION

FIELD-ORIENTED control (FOC) of three-phase ac machines has demonstrated itself in terms of control stability and dynamic performance. Machine real-time rotor position is required to synchronize the commutation of all power electronic devices. However, a system with a rotor position sensor has the following drawbacks:

1) signal electromagnetic interference (EMI)/electromagnetic compatibility;
2) extra step for rotation direction and sensor offset detection;
3) hardware cost and reliability degradation;
4) cable wiring, installation, and packaging space.

On the other hand, FOC operation without a position sensor (or sensorless control) shows its advantage due to its "plug and play" convenience. There have been tremendous research interests and efforts designated for sensorless operation over the years. Early on, position sensorless control is treated as the backup solution for sensor-based drives when position sensor failure occurs. For certain safety-critical applications, uninterrupted drive operation is essential even when the sensor fails. This is normally denoted as operation in "fail-safe mode" or "limp mode." The continued increases in microprocessor real-time processing power speed up the adoption of full-speed sensorless control over time. Sensorless operation becomes a de facto "out-of-box" configuration in certain applications. It is reported that a servo drive equipped with sensorless technology can achieve $\pm 1.8°$ position control precision [1].

A variety of sensorless control methods, i.e., driving synchronous machines, has been proposed both in academia and industry. Fig. 1 shows the common classification of different sensorless control algorithms. The common sensorless technologies fall into two major categories: one looks at stator winding back electromotive force (back EMF) voltage induced by rotor movement and the other examines inductance variation along rotor peripheral. The back EMF method can be further divided into fundamental back EMF voltage [2]–[4] and third harmonics

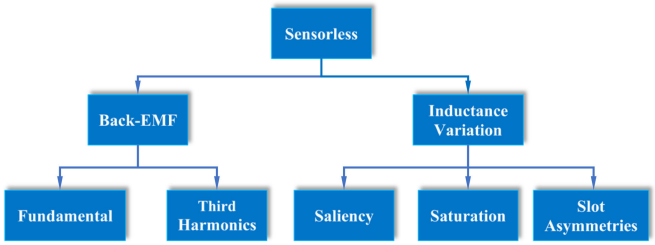

Fig. 1. Sensorless control algorithm classification.

back EMF voltage [5], [6]. Inductance variation could be initiated by either rotor geometry anisotropy (saliency), saturation induced by excessive current, or slot asymmetry [7]–[9]. For sensorless based on inductance variation, high-frequency injection (HFI) is the commonly used technique, which detects rotor position using rotor saliency. Three common injection methods, i.e., the sinusoidal waveform injection [10], the pulsating voltage injection [11], [12], and the square waveform injection [13], are reported based on where and what signal is injected. Fig. 2 shows the frequency domain that can be divided into a few sections that take account of different methods and frequency components.

Position sensorless control using advanced observers, such as sliding mode observer (SMO) [14]–[16] and extended Kalman filter (EKF) [17]–[19], has been investigated and validated. In recent years, researchers focus on the continuous performance improvement of these sensorless control algorithms. Research works in [20]–[25] proposed methods to reduce the phase delay and speed chattering associated with SMO. Research works in [26] and [27] visited several special types of observers such as unscented Kalman filter and Bobtsov's observer.

This article tries to compare and classify back EMF based sensorless control schemes qualitatively using several criteria. Dealing with back EMF sensorless control has a unique challenge because FOC current control and position estimation scheme manipulate the same fundamental frequency component. The cross-coupling effect makes the design and tuning of the whole system difficult. Sensorless control using back EMF voltage has been reviewed by several literature [2], [28]–[36]. The performance of different back EMF based sensorless schemes has been experimentally validated. Table I summarizes the steady-state and transient performance of a few typical methods. However, most literature evaluate sensorless control from a machine electromagnetic perspective. The inherent connections and classifications among different algorithms have not been explored in-depth mathematically. This article targets to summarize and classify different back EMF based sensorless schemes established upon mathematical control models and theories. Fig. 3 shows different types of synchronous machine in terms of torque production mechanism. In this article, synchronous machine mainly refers to synchronous permanent magnet (PM) and reluctance machine excluding dc excited synchronous machine. For analysis without loss of generality, the mathematical model of an interior permanent magnet (IPM) machine is used although the same analysis applies to all synchronous machines.

This article is organized as follows. In Section II, a synchronous machine plant model and its FOC control with and without position sensor are evaluated from the system level. Once established, the standard synchronous machine mathematical model and two adjusted model variants for sensorless control are presented in Section III. Then, the basic back EMF based sensorless algorithms are reviewed. Following that, Section IV reviews the observer theory and its two typical implementation forms. Sections V and VI review sensorless algorithms in both stationary reference frame (StatRF) and synchronous reference frame (SyncRF). The specialty of each algorithm and inherent connections between different algorithms are investigated. Section VII concludes and categorizes different sensorless algorithms using the proposed five criteria. A conclusion is given in Section VIII to highlight the contributions of this article.

TABLE I
BACK EMF SENSORLESS METHODS PERFORMANCE SUMMARY

Method	Author	Steady State and Transient Performance
Stator observer using extended-EMF	Z. Chen [3]	• maximum position error 1°. • maximum velocity control error 2% of command velocity. • velocity estimation error does not increase very much at accelearionts and deceleration.
Stator observer using active flux	I. Boldea [2]	• Successful ±1 speed reversal with 100% step-torque transient at 1 rpm. • Maximum speed 4000rpm vs base speed at 1000rpm.
Stator observer using active flux	G. Foo [37]	• Low-speed reversal from -10 (6.67‰) to +10 rpm. • Zero speed with rated torque stable. • 0.1 sec, 0 speed to 1000rpm (66.7%).
Sliding mode	C. Song[14]	• 50 r/min (20%) and 1000 r/min (400%) 10Nm and 2Nm.
Observer using current regulator output	B. H. Bae [55]	• Acceleration from 58000r/min(82.85%) to 60000r/min(85.71%). • Stable operation at 65000 r/min(92.86%) with 120kW(91.6%).
Adaptive observer	N. Matsui [72]	• Position estimation errors are less than 2°. • Zero-speed control has been achieved for a 0% - 100% load torque. • Position estimation error is whtin 5° during transient state.
Extended-EMF in rotating reference frame	S. Morimoto [4]	• Both an estimation position error and an estimtion speed error are very small. • A stable operation cannot be obtained below 100 r/min. • A step change of 100% load torque, the estimation position error and estimation speed error reach 15° and 40 r/min.

II. VECTOR CONTROL WITH AND WITHOUT POSITION SENSOR

A synchronous machine and its control algorithm can be modeled using block diagrams shown in Fig. 4, which includes machine electrical subsystem (purple background), mechanical subsystem (yellow background), and control subsystem (green background). The control subsystem can further be divided into current control loop, voltage feedforward, and position sensor or sensorless algorithm. A toggle switch is used to change control modes between position-sensored control and position-sensorless control.

A. Plant Diagram

In Fig. 4, the right half depicts a machine model with both electrical and mechanical subsystems. The electrical system

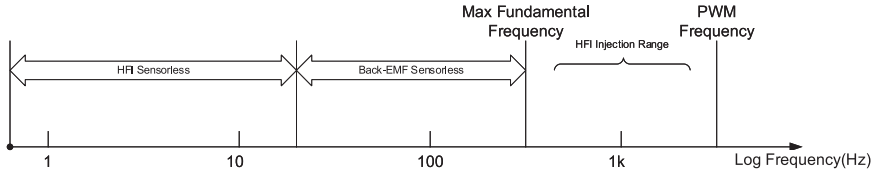

Fig. 2. Sensorless control frequency domain for various components.

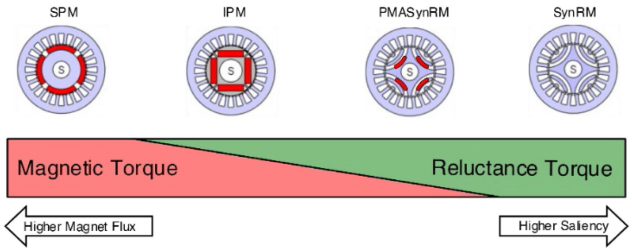

Fig. 3. Different types of synchronous machines and their torque generation mechanisms.

is modeled in rotor flux-oriented dq SyncRF. Torque equation block (Trq) connects electrical side to mechanical side, whereas mechanical side couples back to electrical side via actual rotor position θ and speed ω. External disturbance is injected through load torque T_L (①). This disturbance propagates to electrical side through rotor speed (③) and rotor position (④). In Fig. 4, these mutual coupling loops are highlighted using solid red line and solid blue line. These machine internal loops are nonlinear due to input voltage V_{abc} $3s/2r$ conversion and dual dq axes electric subsystem to single-axis mechanical system conversion. As a result, finding analytical transfer functions that describe overall plant dynamics becomes challenging. Nevertheless, the transfer functions of the blocks in the forward path provides a reasonable estimate. The path from input voltage to output speed ω consists of two cascaded integrators as $1/s^2$, while the path from input voltage to output position θ is a function of $1/s^3$. Normally, high order plant model indicates long system time constant and potential resonance. For controller design, a good practice is to decouple mechanical and electrical loops, which is shown using red and blue crosses in Fig. 4. Once finished, both electrical side and mechanical side only need to design a controller to manipulate a first order system. For example, the disturbance from load torque can be easily rejected by a speed regulator without affecting electrical side.

B. Decoupling Control With Position Sensor

In Fig. 4, the left half in green background highlights FOC control block diagrams inside a microprocessor. To achieve decoupled control between electrical and mechanical sides, FOC is invented that aligns the control axis toward rotor flux based on real-time speed/position feedback. In Fig. 4, a switch is used to select either sensor feedback or sensorless estimation. For control with a position sensor, speed/position information is extracted via the position sensor. This signal path is highlighted in red dash dot line (line ②). The position is used by the transformation block (line ⑥), which rejects disturbance introduced from mechanical side to electrical side through θ (line ④) inside the machine. Meanwhile, the speed coupling (line ③) inside the machine is decoupled by adding the speed-related machine electrical model to the output of the current PI regulator (line ⑦). As a result, speed outer loop (not shown in Fig. 4) and dq current inner loops can be separately designed with adequate bandwidth margin.

C. Decoupling Control Without Position Sensor

Position signal feedback introduces a few issues acknowledged in Section I. Position sensorless control is therefore designed to implement FOC control without a position sensor. The blue dash line in Fig. 4 highlights the position estimation path for sensorless FOC control. In this case, plant disturbance is detected through sampled three-phase currents (line ⑤). A position & speed observer is built to estimate rotor position and speed information from inverter command voltage and sampled current signals. Once the position and speed are obtained, the same decoupling process (⑥ and ⑦) described above is adopted. Consequently, FOC control can still be maintained by properly designing the "Position & Speed Observer." A well-designed sensorless algorithm could potentially replace the position sensor without compromising system overall performance.

III. Synchronous Machine Modeling and Existing Methods

This section provides the mathematical model of a synchronous machine and two of its model variants that facilitate sensorless control algorithm design. Based upon these models, the motor initial rotor angle detection schemes and basic back EMF based sensorless methods are reviewed.

A. Modeling of a Synchronous Machine

A synchronous machine (or an IPM) is described by the following voltage equation in dq SyncRF:

$$\begin{bmatrix} v_d \\ v_q \end{bmatrix} = \begin{bmatrix} R_s + pL_d & -\omega_r L_q \\ \omega_r L_d & R_s + pL_q \end{bmatrix} \begin{bmatrix} i_d \\ i_q \end{bmatrix} + \begin{bmatrix} 0 \\ \omega_r \lambda_m \end{bmatrix}. \quad (1)$$

It can be converted into $\alpha\beta$ StatRF as

$$\begin{bmatrix} v_\alpha \\ v_\beta \end{bmatrix} = \begin{bmatrix} L_0 + L_1 \cos(2\theta_e) & L_1 \sin\theta_e \\ L_1 \sin\theta_e & L_0 - L_1 \cos(2\theta_e) \end{bmatrix} \cdot \frac{d}{dt} \begin{bmatrix} i_\alpha \\ i_\beta \end{bmatrix} + R_s \begin{bmatrix} i_\alpha \\ i_\beta \end{bmatrix} + \omega_r \lambda_m \begin{bmatrix} -\sin\theta_e \\ \cos\theta_e \end{bmatrix}. \quad (2)$$

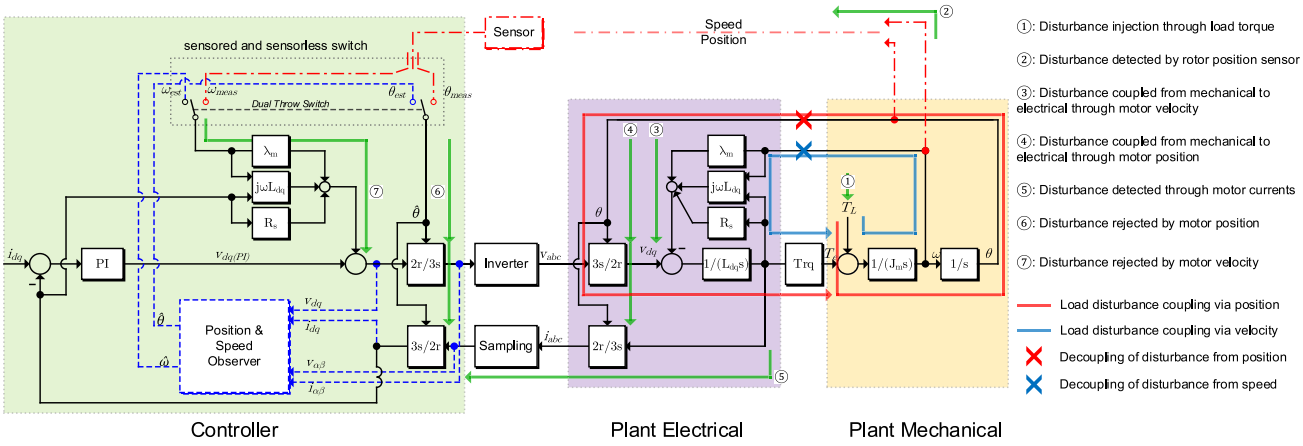

Fig. 4. Synchronous machine plant and control model in *dq* coordinate.

In (2), both back EMF voltage and current derivative coefficient are a function of rotor position θ_e. This mainly is attributed to the diagonal asymmetry of the current vector coefficient matrix in (1) [3]. Considering a nonsalient surface-mounted PM (SPM) machine where its L_d and L_q are both equal to L_0, (1) and (2) can be converted to

$$\begin{bmatrix} v_d \\ v_q \end{bmatrix} = \begin{bmatrix} R_s + pL_0 & -\omega_r L_0 \\ \omega_r L_0 & R_s + pL_0 \end{bmatrix} \begin{bmatrix} i_d \\ i_q \end{bmatrix} + \begin{bmatrix} 0 \\ \omega_r \lambda_m \end{bmatrix} \tag{3}$$

$$\begin{bmatrix} v_\alpha \\ v_\beta \end{bmatrix} = (R_s + pL_0) \begin{bmatrix} i_\alpha \\ i_\beta \end{bmatrix} + \omega_r \lambda_m \begin{bmatrix} -\sin\theta_e \\ \cos\theta_e \end{bmatrix}. \tag{4}$$

Equation (4) shows that rotor position θ_e can be back-calculated using stator voltage vector $[v_\alpha\ v_\beta]^T$ and current vector $[i_\alpha\ i_\beta]^T$. However, for a salient pole synchronous machine such as an IPM machine, it is not possible to calculate θ_e directly by using (2).

To retrieve the convenience for theta calculation for a saliency pole synchronous machine, two model variants are proposed that removes θ_e and $2\theta_e$ from the coefficient matrix before the current derivative term $\frac{d}{dt}[i_\alpha\ i_\beta]^T$ in (2).

B. Model Variants of Salient Pole Synchronous Machines for Sensorless Control

1) Extended EMF: Equation (1) is rewritten as

$$\begin{bmatrix} v_d \\ v_q \end{bmatrix} = \begin{bmatrix} R_s + pL_d & -\omega_r L_q \\ \omega_r L_q & R_s + pL_d \end{bmatrix} \begin{bmatrix} i_d \\ i_q \end{bmatrix} + \begin{bmatrix} 0 \\ E_{\text{ex}} \end{bmatrix} \tag{5}$$

where E_{ex} in (5) is known as "Extended EMF." It is expressed as

$$E_{\text{ex}} = (L_d - L_q)\left(\omega_\lambda i_d - \dot{i}_q\right) + \omega_\lambda \lambda_m. \tag{6}$$

Converting (5) into $\alpha\beta$ StatRF yields

$$\begin{bmatrix} v_\alpha \\ v_\beta \end{bmatrix} = \begin{bmatrix} R_s + pL_d & \omega_r (L_d - L_q) \\ -\omega_r (L_d - L_q) & R_s + pL_d \end{bmatrix} \begin{bmatrix} i_\alpha \\ i_\beta \end{bmatrix} + E_{\text{ex}} \begin{bmatrix} -\sin\theta_e \\ \cos\theta_e \end{bmatrix}. \tag{7}$$

Now, only the extended EMF on the right-hand side of (7) is θ_e related.

2) Active Flux: Equation (1) is rewritten as

$$\begin{bmatrix} v_d \\ v_q \end{bmatrix} = \begin{bmatrix} R_s + pL_q & -\omega_r L_q \\ \omega_r L_q & R_s + pL_q \end{bmatrix} \begin{bmatrix} i_d \\ i_q \end{bmatrix} + \begin{bmatrix} \frac{d\lambda^{af}}{dt} \\ \omega_r \lambda^{af} \end{bmatrix}. \tag{8}$$

λ^{af} in (8) is defined as "Active Flux" [2] or "Extended Rotor Flux" [37] or "Equivalent EMF" [38]. It is expressed as

$$\lambda^{af} = \lambda_m + (L_d - L_q)\, i_d. \tag{9}$$

Approximating active flux in (9) as a constant, equation (8) is converted into $\alpha\beta$ StatRF with rotor θ_e only appearing on the back EMF term as

$$\begin{bmatrix} v_\alpha \\ v_\beta \end{bmatrix} = (R_s + pL_q) \begin{bmatrix} i_\alpha \\ i_\beta \end{bmatrix} + \omega_r \lambda^{af} \begin{bmatrix} -\sin\theta_e \\ \cos\theta_e \end{bmatrix}. \tag{10}$$

Given $\lambda^{af} \neq 0$, rotor angle can be retrieved similar to a nonsalient SPM machine model in (4).

Hitherto, (7) and (10) are formulated similarly to (4) with θ_e only existing on the back EMF term. These machine model variants are mainly targeting for sensorless control in StatRF.

C. Initial Rotor Position Detection Methods

Initial rotor position is needed to smoothly start synchronous machines using a back EMF based sensorless control method. Otherwise, a large current transient can be induced which could potentially fault the drive. If the HFI method is adopted at low speed, a PM motor only needs to identify the north/south pole instead of the exact rotor initial position and a synchronous reluctance motor does not require the initial rotor position. There are several ways of identifying the initial position.

1) Aligning the Rotor to a Predefined Position: The rotor can be attracted to a predefined position by injecting a current. The current can be manipulated by closed-loop current control or simply an open-loop gate pattern [39]. However, this method can have initial rotor movement and also the reliability of this method is affected by the load stall torque.

2) Using V/Hz Open-Loop Start-Up Scheme: Open-loop start-up scheme targets to accelerate the motor following a given speed acceleration profile [40]. The open-loop V/Hz control is maintained until reaching a given threshold speed, where transits to a back EMF based sensorless algorithm is reliable. However, the selection of acceleration profile is critical to minimize potential speed and current oscillations. Meanwhile, the motor usually does not operate at the most efficient point during this period.

3) Initial Rotor Position Detection by Inductance Variation: Fig. 3 shows different types of synchronous machine. For a synchronous machine with reluctance torque capability, the rotor position can be detected within 180° electric angle by inductance variation. To further determine the south/north pole position of an SPM/IPM machine, a large current pulse is injected to saturate the rotor intentionally. Injecting the current vector along the north pole will lead to a higher saturation level than injecting along the south pole, which also induces inductance variation. A few initial rotor position detection schemes using this inductance variation are reported [41]–[44].

D. Sensorless Control Methods Using Back EMF

After merging all θ_e related terms into back EMF terms in (7) and (10), rotor position is derived directly through calculation using $\alpha\beta$ axes voltage equation. However, it is less desirable to perform direct derivative calculation toward feedback current in (4), (7), and (10) considering the noise generated from the calculation. Two alternative methods are applied to eliminate derivative operation.

1) Position Estimation Through Calculating Flux Linkage Angle: Instead of calculating the back EMF voltage angle, a rotor flux angle which lags back EMF voltage by 90° is calculated by performing integration toward the voltage equation. The stator flux linkage is then interpreted as

$$\begin{cases} \lambda_{s\alpha} = \int (v_\alpha - R_s i_\alpha)\, dt \\ \lambda_{s\beta} = \int (v_\beta - R_s i_\beta)\, dt \end{cases}. \tag{11}$$

The rotor flux linkage is calculated by subtracting stator armature flux linkage from (11) as

$$\begin{cases} \lambda_{r\alpha} = \lambda_{s\alpha} - L_0 i_\alpha \\ \lambda_{r\beta} = \lambda_{s\beta} - L_0 i_\beta \end{cases}. \tag{12}$$

For a salient pole machine, the active flux in Section III-B2 is given as

$$\begin{cases} \lambda_\alpha^{af} = \lambda_{s\alpha} - L_\mathrm{q} i_\alpha \\ \lambda_\beta^{af} = \lambda_{s\beta} - L_\mathrm{q} i_\beta \end{cases}. \tag{13}$$

Rotor position is retrieved by calculating rotor flux angle directly from (12) or (13) as

$$\theta_e = a\tan\left(\frac{\lambda_{r\beta}}{\lambda_{r\alpha}}\right) \; or \; \theta_e = a\tan\left(\frac{\lambda_\alpha^{af}}{\lambda_\beta^{af}}\right). \tag{14}$$

However, direct integration calculation introduces dc drift in (11). A high-pass filter (HPF) is typically used to remove the dc drift

$$\lambda_s^{\mathrm{HPF}} = \frac{s}{s+\omega_\lambda}\,\lambda_s \tag{15}$$

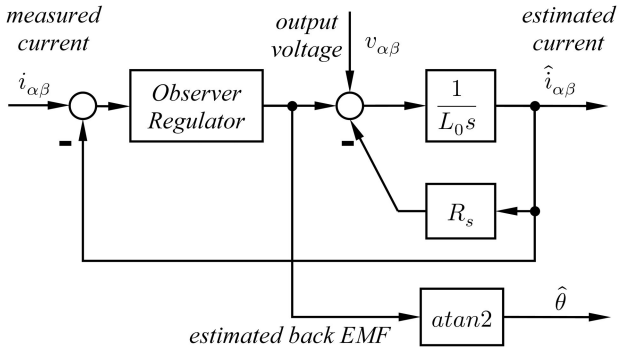

Fig. 5. Position sensorless control using an observer in StatRF.

where ω_λ is the HPF cutoff frequency.

HPF introduces phase leading at low operational frequency, for example, the frequency below ω_λ. Usually, angle detection at low speed is augmented with the HFI method so full speed range sensorless control is achieved.

This flux linkage based direct rotor angle calculation method is categorized as "open-loop calculation" in some of the published literature [2], [28]–[36]. This will be further reviewed in later sections.

2) Position Estimation Through Back EMF Voltage in StatRF: Rotor position is embedded within back EMF voltage. An "observer" is constructed to estimate it from known plant inputs and outputs. An observer is first formulated in StatRF based upon either (4), (7), or (10). Equation (4) is used as an example and its observer implementation is shown in Fig. 5. Estimated rotor position $\hat{\theta}$ is then derived from estimated back EMF voltage as

$$\begin{aligned} \hat{\dot{i}}_\alpha &= \frac{1}{L_0}\int \left(v_\alpha - R_s \hat{i}_\alpha - \mathrm{EMF}_\alpha\right) \\ \hat{\dot{i}}_\beta &= \frac{1}{L_0}\int \left(v_\beta - R_s \hat{i}_\beta - \mathrm{EMF}_\beta\right) \end{aligned} \tag{16}$$

$$\begin{aligned} \mathrm{EMF}_\alpha &= f\left(i_\alpha - \hat{i}_\alpha\right) \\ \mathrm{EMF}_\beta &= f\left(i_\beta - \hat{i}_\beta\right) \end{aligned} \tag{17}$$

$$\hat{\theta} = a\tan 2\left(\frac{\mathrm{EMF}_\alpha}{\mathrm{EMF}_\beta}\right) \tag{18}$$

where $f()$ in (17) represents the function of the observer regulator in Fig. 5. $a$tan2 in (18) is the modified arctangent function, which returns an angle between $[-\pi, \pi]$. The conventional arctangent function can only tell the angle between $[-\frac{\pi}{2}, \frac{\pi}{2}]$.

3) Position Estimation Through Back EMF Voltage in SyncRF: An observer can also operate in SyncRF by referencing (1), (5), and (8). Equation (1) in SyncRF is expanded as an example. Fig. 6 is the observer form of the control diagram for the equation. A phase-locked loop (PLL) is used to extract speed and position information from error between measured current i_{dq} and estimated current $\hat{i}_{dq}$. In Figs. 5 and 6, if only proportional gain is applied to observer regulator, this is popularly known as Luenberger observer [45].

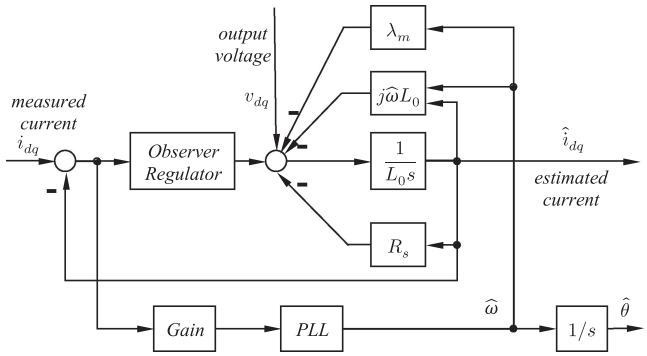

Fig. 6. Position sensorless control using an observer in SyncRF.

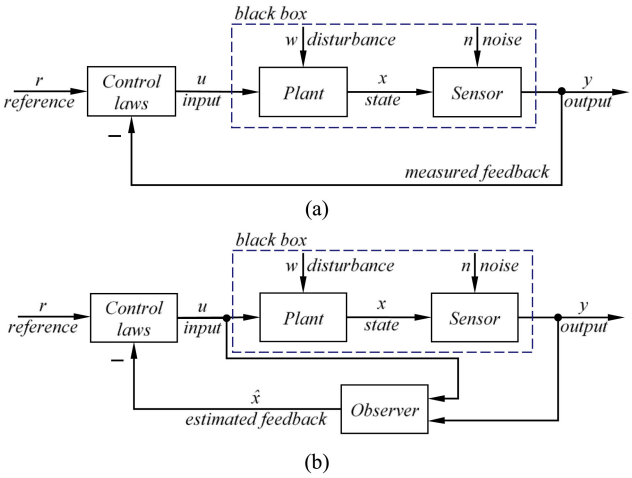

Fig. 7. Measuring states. (a) Sensors measure states. (b) Observer estimates states.

An in-depth analysis will be covered regarding the difference between observers implemented in StatRF versus SyncRF in Sections V and VI.

IV. Observer and Its Two Implementation Forms

Observer is used to extract real-time information from dynamic systems using input and output data. It can replace or augment sensors, provide less expensive, more reliable solutions, and can estimate unmeasurable signals [45]–[48]. Fig. 7 compares the control loop using a sensor versus using an observer. Based on the source for the observer inputs, observers can be divided into three categories, which are illustrated in Table II. For electric machine sensorless control, an observer is used to estimate mechanical rotor position from electrical signals without a position sensor.

A. Observer Internal Model Observer (IMO) Form Versus Filter Form

The "Plant Input and Output Observer" in Table II serves as the base set for a modern observer. It has two forms of fulfillment, the IMO form (or loop form) and the filter form [49]. IMO form is normally how an observer is implemented, whereas filter

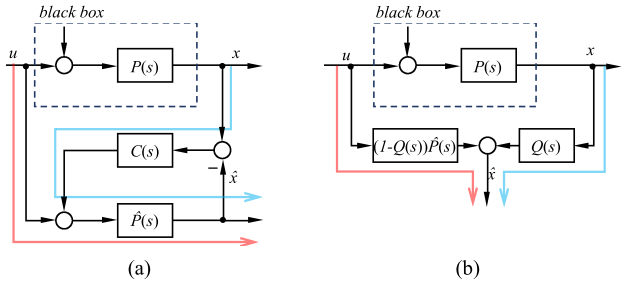

Fig. 8. Luenberger observer. (a) IMO form. (b) Filter form.

form tells a mathematical equation from plant input and output signals to estimate signal. These two forms are mathematically equivalent. Depending on the estimation target, the IMO form is either named Luenberger observer, which estimates plant state or called disturbance observer, which estimates input disturbance. They are explored separately in the following.

1) Luenberger Observer: Luenberger is designated to estimate plant state x using both the input and output data along with plant information. Fig. 8 shows the IMO form and filter form of a Luenberger observer. In the figure, solid red line denotes signal estimation from plant input, while the solid blue line represents signal estimation from plant sampled output. According to Mason's gain formula and superposition theorem, the estimated state $\hat{x}$ in Fig. 8(a) is a combination of the transfer function from input u and output x as

$$\hat{x} = \frac{P(s)}{1 + C(s)P(s)}u + \frac{C(s)P(s)}{1 + C(s)P(s)}x. \tag{19}$$

Here, plant mathematical model $\hat{P}(s)$ is assumed to be equivalent to actual plant model $P(s)$. The sensor in Fig. 7 and Table II is assumed ideal so that state x and output y are equal.

To simplify (19), the $Q(s)$ filter is defined as

$$Q(s) = \frac{C(s)P(s)}{1 + C(s)P(s)}. \tag{20}$$

The $Q(s)$ filter in (20) is a low-pass filter (LPF) and its transfer function could vary depending on the plant transfer function and observer regulator transfer function. Equation (19) is converted to

$$\hat{x} = \underbrace{\left(\frac{1 - Q(s)}{\text{HPF}}\right)}\underbrace{\frac{P(s)}{\text{model}}}u + \underbrace{\frac{Q(s)}{\text{LPF}}}x. \tag{21}$$

Equation (21) is plotted in Fig. 8(b). Estimated state $\hat{x}$ is sourced from both plant input u and output x. The bandwidth setting of filter $Q(s)$ adjusts the ratio between trusting the model $\hat{P}(s)$ or the measured output x.

2) Disturbance Observer: Sensorless control is to estimate rotor angle, whose information is embedded inside the disturbance coupled from mechanical side to electrical side. Consequently, position can be retrieved from the disturbance instead of the state. Usually, this is entitled "Disturbance Observer." Fig. 9(a) and (b) shows the disturbance observer using both IMO form and filter form. Adopting the same Mason's gain

TABLE II
TYPES OF OBSERVERS

Observer Type	Equivalent Name	Characteristics	Illustration Figure
Plant Output	Filtering the measured output	• Good for measuring low frequencies. • Trust the measurement 100%	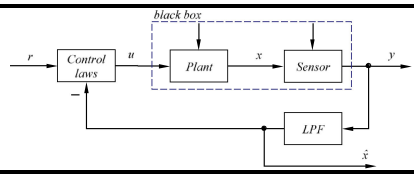
Plant Input	Open loop control	• Good for measuring high frequencies • Trust the model 100%	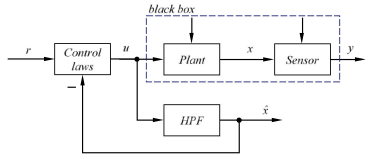
Plant Input Output	Luenberger or Closed Loop Observer	• Trade off between trusting the measurement and trusting the model	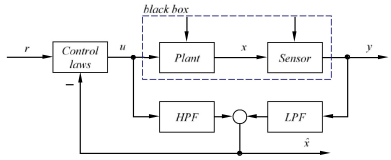

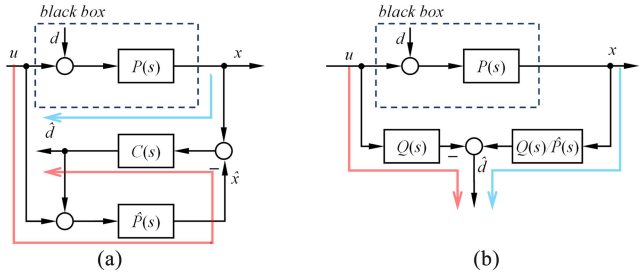

Fig. 9. Disturbance observer. (a) IMO form. (b) Filter form.

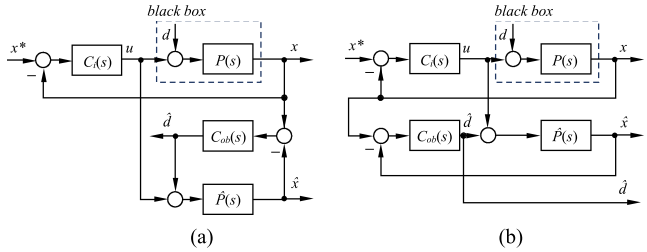

Fig. 10. Observer Layout. (a) Traditional form with emphasis on plant model. (b) Adopted form with emphasis on observer regulator.

formula and superposition theorem, the estimated disturbance is expressed as

$$\hat{d} = \frac{C(s)P(s)}{1+C(s)P(s)}(-u) + \frac{C(s)}{1+C(s)P(s)}x. \tag{22}$$

With the same $Q(s)$ filter definition in (20), (22) is rewritten as

$$\hat{d} = \underbrace{Q(s)}_{\text{LPF}}(-u) + \underbrace{Q(s)}_{\text{LPF}}\underbrace{P(s)^{-1}}_{\text{model}}x = \underbrace{Q(s)}_{\text{LPF}}\left(-u + P(s)^{-1}x\right). \tag{23}$$

The estimated disturbance $\hat{d}$ is a function of input u and output x. Observer regulator $C(s)$ determines the type and bandwidth of $Q(s)$ filter. Assuming the plant model to be a pure inductor with $P(s) = \frac{1}{Ls}$ and proportional observer gain $C(s) = k$, $Q(s)$ filter in (20) is expressed as

$$Q(s) = \frac{1}{\frac{L}{k}s+1}. \tag{24}$$

The disturbance estimation is dictated by substituting (24) into (23) as

$$\hat{d} = \frac{1}{\frac{L}{k}s+1}(-u) + \frac{1}{\frac{L}{k}s+1}(Lsx) = \frac{1}{\frac{L}{k}s+1}(-u+Lsx). \tag{25}$$

Once the disturbance observer is converted to a filter form in Fig. 9(b) from IMO form in Fig. 9(a), the estimated state $\hat{x}$ is no longer accessible.

B. Observer Regulator Versus Command Regulator

Fig. 10 shows different observer layouts within the control system. Fig. 10(a) shows the widely adopted approach, where observer regulator $C_{ob}(s)$ is applied toward the difference between measured state x and estimated state $\hat{x}$. In Fig. 10, the command signal regulator $C_i(s)$ (e.g., a current regulator for a machine) is added to the system for comparison. Different than Fig. 10(a), the observer regulator $C_{ob}(s)$ in Fig. 10(b) is rearranged parallel toward signal regulator $C_i(s)$. Instead of handling the actual plant $P(s)$, the observer regulator $C_{ob}(s)$ controls estimated plant model $\hat{P}(s)$. The difference is $C_i(s)$ works on the error between command x^* and feedback x, whereas $C_{ob}(s)$ manipulates error between feedback x and estimate $\hat{x}$. Theoretically, regulator used by $C_i(s)$, whether it is a "PID," or a "resonant," or a "model predictive," or even a "sliding mode" controller, should be applicable to $C_{ob}(s)$ likewise. In Fig. 10(b), the observer regulator outputs the estimated plant disturbance $\hat{d}$, which is added to command regulator output u. The total signal drives the estimated state $\hat{x}$ toward the actual plant state x. The

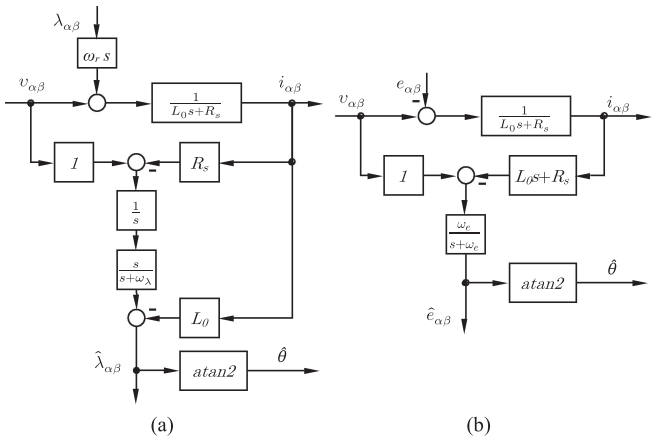

Fig. 11. Sensorless method in observer representation. (a) Flux calculation method in Section III-C1. (b) Back EMF method in Section III-C2.

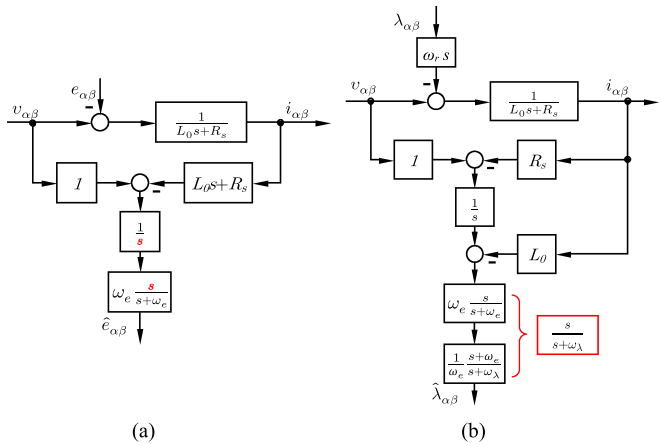

Fig. 12. Developed from of observer in StatRF. (a) Divided LPF. (b) Convert the estimated back EMF output $\hat{\boldsymbol{e}}_{\boldsymbol{\alpha\beta}}$ into rotor flux output $\hat{\boldsymbol{\lambda}}_{\boldsymbol{\alpha\beta}}$.

benefit of Fig. 10(b) is supporting a balanced view toward the command control loop and the observer loop.

V. Sensorless Control in Stationary Reference Frame

Sections III and IV introduce the basics of motor sensorless control and observer. In this section, observer theory will be utilized to explain fundamental connections between different sensorless methods in StatRF. As mentioned previously, most literatures characterize flux linkage based sensorless control method elaborated in Section III-C1 as an open-loop calculation method [2], [28]–[36]. In this section, the observer representation of sensorless control using flux linkage calculation is explored. The connection between two basic sensorless methods in Section III-C1 and Section III-C2 is explained.

Since the voltage equation for a nonsalient pole machine model in (4) and that for a salient pole machine model in (10) using the active flux model variant are close to each other, the stator inductance L_0 for a nonsalient pole machine is used below where it can always switch to L_q for a salient pole machine.

A. Position Estimation Through Flux Linkage Versus Back EMF

Equations (11)–(15) formulate a sensorless angle detection method using calculated rotor flux linkage. They can be translated into control block diagram shown in Fig. 11(a). The estimated angle is a function of both machine input $v_{\alpha\beta}$ and output $i_{\alpha\beta}$. According to the definition of observer types in Table II, this should belong to "Plant Input and Output Observer" or "Closed-Loop Observer" rather than the "Open Loop Calculation" method.

Alternatively, sensorless control using an observer in StatRF is defined using (16)–(18) and Fig. 5. The observer theory in Section IV indicates that Fig. 5 is the IMO form of an observer. It can be converted into a filter form shown in Fig. 11(b), considering only proportional gain applied for observer regulator. Here, ω_e denotes the bandwidth of LPF.

B. Similarities and Differences Between Flux Calculation Method and Back EMF Method

When observing Fig. 11(a) and (b), they share a handful of common elements. This leads to the speculation that these two sensorless methods are the same method expressed in two different ways rather than two different methods. This is explored and expanded in the following paragraphs.

First, the LFP block $\frac{\omega_e}{s+\omega_e}$ in Fig. 11(b) can be split into two separate blocks $\frac{1}{s}$ and $\omega_e \frac{s}{s+\omega_e}$ shown in Fig. 12(a). In Fig. 12(a), the derivative operation inside block $L_0 s + R$ can be moved after integration block $\frac{1}{s}$. A separate branch L_0 is created and added to the output of $\frac{1}{s}$ shown in Fig. 12(b). Disturbance and angle estimated in Fig. 11(b) is built upon estimated back EMF voltage $\hat{e}_{\alpha\beta}$, whereas the flux linkage method shown in Fig. 11(a) is built upon estimated rotor flux linkage $\hat{\lambda}_{\alpha\beta}$. The basic electromagnetics theory tells flux angle lags its induced voltage by 90°, and the corresponding voltage magnitude is scaled down by signal frequency to derive flux magnitude. The following equation then holds

$$\hat{\lambda} = \hat{e} \cdot \frac{e^{j\left(-\frac{\pi}{2}\right)}}{\omega_r}. \tag{26}$$

In (26), the 90° delay $e^{j\left(-\frac{\pi}{2}\right)}$ can be approximated by a lag–lead filter as

$$\frac{e^{j\left(-\frac{\pi}{2}\right)}}{\omega_r} \approx \frac{1}{\omega_e}\frac{s+\omega_e}{s+\omega_\lambda}. \tag{27}$$

To verify (27), the Bode plot for both sides of (27) is shown in Fig. 13. For illustration purposes, frequencies such as HPF bandwidth ω_λ, LPF bandwidth ω_e, and fundamental frequency ω_r are set to 2Hz, 1000 Hz, and 100 Hz. In the figure, the blue line represents the Bode plot for $\frac{e^{j\left(-\frac{\pi}{2}\right)}}{\omega_r}$. The red line denotes Bode plot for $\frac{1}{\omega_e}\frac{s+\omega_e}{s+\omega_\lambda}$. Fig. 13 shows two magnitude curves intersect exactly at fundamental frequency ω_r, whereas phase curves are quite different at different frequency points. The closer the fundamental frequency ω_r gets toward either

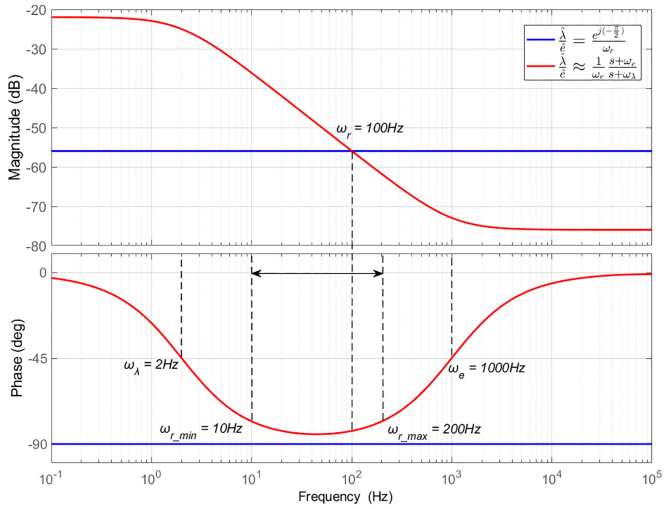

Fig. 13. Bode plots of $\frac{e^{j(-\frac{\pi}{2})}}{\omega_r}$ and $\frac{1}{\omega_e}\frac{s+\omega_e}{s+\omega_\lambda}$ in (27).

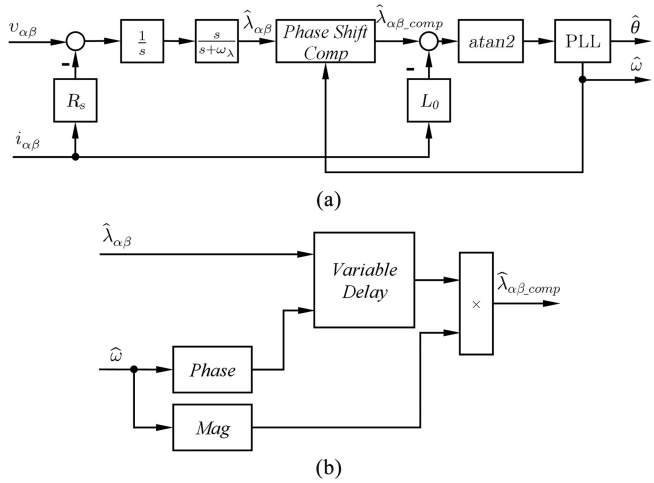

Fig. 15. Filter phase shift compensation block diagram. (a) Phase shift compensation block within sensorless control loop. (b) Expanded view of phase shift compensation block.

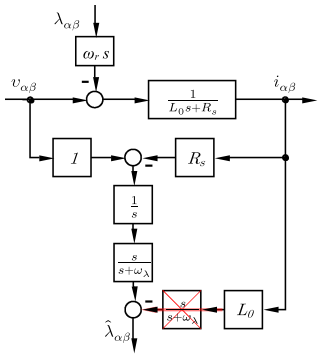

Fig. 14. Developed form of the back EMF method with $\frac{s}{s+\omega_\lambda}$ moving upstream.

HPF bandwidth ω_λ or LPF bandwidth ω_e, the larger the phase angle difference is. This phase error determines angle estimation difference between these two methods. In Fig. 13, the motor fundamental operation frequency is restricted from $\omega_{r\_\min} = 10$ Hz to $\omega_{r\_\max} = 200$ Hz for the purpose of making approximation in (27) valid.

By connecting block $\frac{1}{\omega_e}\frac{s+\omega_e}{s+\omega_\lambda}$ to the estimated back EMF $\hat{e}_{\alpha\beta}$ in Fig. 12(a), the final estimated disturbance becomes $\hat{\lambda}_{\alpha\beta}$ as shown in Fig. 12(b). In Fig. 12(b), blocks $\omega_e\frac{s}{s+\omega_e}$ and $\frac{1}{\omega_e}\frac{s+\omega_e}{s+\omega_\lambda}$ can be further simplified to $\frac{s}{s+\omega_\lambda}$ as highlighted using red square. This $\frac{s}{s+\omega_\lambda}$ is the same HPF that is used in Fig. 11(a), which is designated for removing dc drift due to integration operation. By moving block $\frac{s}{s+\omega_\lambda}$ upstream to both $\frac{1}{s}$ and L_0 signal paths, Fig. 12(b) is converted into Fig. 14. In Fig. 14, considering a minimum speed that the back EMF method can apply, block $\frac{s}{s+\omega_\lambda}$ in L_0 path can approximate to a unity gain, which is highlighted using the red solid line. Sensorless angle detection method established upon flux linkage calculation in Fig. 11(a) and the developed block diagram of the back EMF based observer method shown in Fig. 14 are now identical. In short, the flux calculation sensorless method in Section III-C1 and Fig. 11(a) and the observer sensorless method in Section III-C2 and Fig. 11(b) are mathematically equivalent considering the validity of (27).

However, the HPF block $\frac{s}{s+\omega_\lambda}$ in Fig. 11(a) causes phase leading at low operational speed and the LPF block $\frac{\omega_e}{s+\omega_e}$ in Fig. 11(b) generates phase lagging at high operational speed. Both methods calculate the estimated angles that approximate actual rotor angle. In summary, the flux linkage sensorless method is more useful at high speed while the back EMF based method is more reliable at low speed (exclude near zero speed where there is no back EMF voltage for reliable angle detection).

C. Rotor Angle Estimation Phase Error

The basic sensorless methods above exhibit angle deviation as the fundamental frequency moves closer to filter cutoff frequency. This phase error causes drive performance degradation since the motor rotor flux field is not properly oriented [50]. There are a few ways to address this issue.

1) Filter Phase Shift Compensation: The filter phase shift can be compensated as the transfer function of the filter is already known. However, the compensation is accurate only during steady-state operation. This could be an issue for a process with high dynamics. In addition, the compensation is a direct function of estimated rotor speed. In other words, the output affected by compensation feeds back as compensation input, which results in an algebraic loop. Although a delay block can be inserted to break up the loop, this compensation may only work for systems with slow dynamics.

Fig. 15 shows a typical filter phase shift compensation block used for flux linkage-based position estimation. Fig. 11(a) is the original sensorless implementation, and Fig. 15(a) adds "Phase Shift Comp" block to the estimated stator flux $\hat{\lambda}_{\alpha\beta}$. This phase shift compensation block tries to compensate the phase and magnitude deviation caused by the HPF $\frac{s}{s+\omega_\lambda}$. The detailed implementation of "Phase Shift Comp" block is expanded in Fig. 15(b). Since the transfer function of HPF is known, the

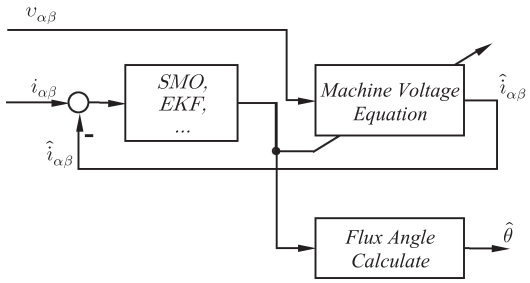

Fig. 16. Observer regulator using a higher order filter or nonlinear gain.

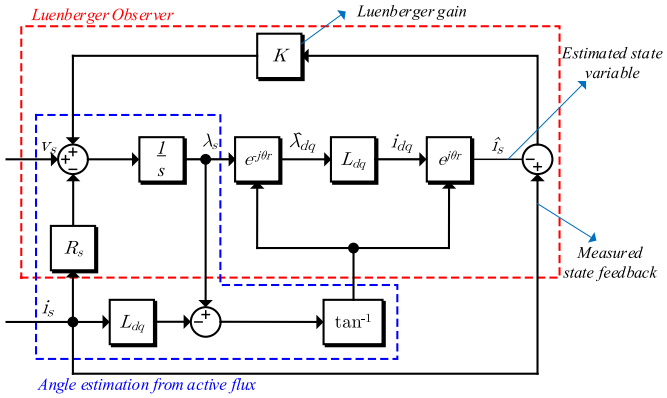

Fig. 17. Position sensorless control algorithm proposed in [37].

phase and magnitude are compensated in Fig. 15(b) either by mathematical equations or by lookup tables. The estimated speed $\hat{\omega}$ from the output of the PLL in Fig. 15(a) is used to decide the compensation in Fig. 15(b).

2) Observer Using a Higher Order Filter or Nonlinear Gain: A higher order filter possesses a steeper Bode curve around cutoff frequency thus less angle deviation. However, the commissioning of multiple coefficients can be cumbersome. In literature, researchers prefer adopting observers with nonlinear gains, such as SMO and EKF. Fig. 16 illustrates the structure of these observers. They are the enhanced observers originating from the base set closed-loop observer shown in Table II. These more advanced regulators can alleviate but cannot fully resolve the phase deviation problem.

3) Method Combining Flux Calculation and StatRF Observer: The HPF used in the flux calculation method causes phase leading below a certain speed. An StatRF observer, combined with a flux calculation method, is built, which uses a closed-loop output to trim the flux calculation input [37], [51].

Fig. 17, cited from [37], depicts the overall control scheme. Since (2) cannot be used to build Luenberger observer directly, the calculated flux linkage in StatRF $\hat{\lambda}_s$ is first converted to SyncRF using estimated angle. Stator current is then derived from the calculated flux linkage in *dq* SyncRF. Finally, the current in SyncRF is converted back to StatRF $\hat{i}_s$ using the same estimated angle.

In Fig. 18, a slightly different approach is proposed in [51]. Stator flux estimated λ_{s_i} is retrieved from measured stator current i_s going from StatRF to SyncRF and then back to StatRF.

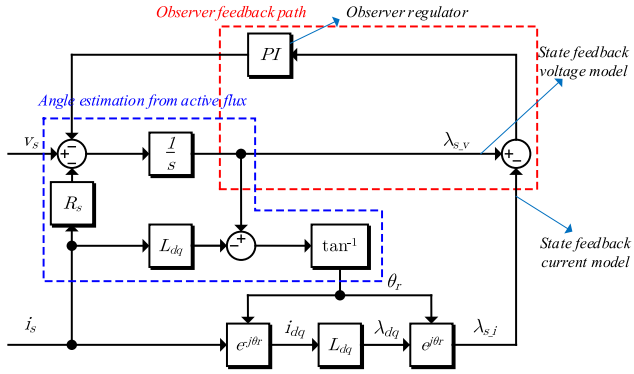

Fig. 18. Position sensorless control proposed in [2] and [51].

4) Observer in Synchronous Reference Frame: The phase deviation is attributed to the fact that all signal processing techniques, whether it is a filter or a regulator, have limited bandwidth and cannot handle signals with variable frequency. Instead of handling variable frequency ac signals in StatRF, they can be converted to dc signals in SyncRF using Park transformation. The analysis of current regulators implemented in both StatRF and SyncRF provides a good reference [52]–[54]. The implementation of an observer in SyncRF is illustrated in Fig. 6. Details regarding various implementations will be reviewed in Section VI.

VI. Sensorless Control in Synchronous Reference Frame

As mentioned in Section III-C3, sensorless control can be implemented in SyncRF. In that case, it does not need to deal with phase shifts associated with ac signal processing. When comparing sensorless control in StatRF versus that in SyncRF, there are following two main differences.

1) Sensorless control in StatRF direct calculates the estimated angle based on a machine mathematical model. Sensorless control in SyncRF checks angle error caused by the difference between the actual machine and machine mathematical model and passes this angle error to a PLL to retrieve the final estimated angle.
2) In addition, sensorless control in StatRF can estimate rotor angle without necessarily feeding it back into the control loop, while sensorless control in SyncRF has to feed the estimated angle into the Park and iPark transformations to make the whole system converge.

A review of existing sensorless control methods in SyncRF is performed to reveal the connections and differences between various methods.

A. Sensorless Methods in SyncRF

For a salient pole machine, sensorless control in StatRF has to work with machine model variants in Section III-B or more precisely (7) and (10). In contrast, sensorless control in SyncRF can use either the original model equation in (1) or model variants in (5) and (8) since none of these equations has a rotor angle dependent coefficient. To better describe different

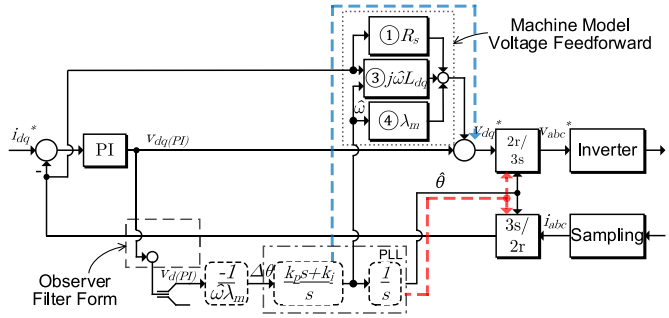

Fig. 19. Sensorless control using current PI regulator outputs.

methods, (1), (5), and (8) are rewritten in the forms of (28), (29), and (30) shown at the bottom of this page, where voltage drop on each item is annotated.

1) Sensorless Control Using Current Loop PI Regulator [55]: Different from reconstructing the machine model in a separate observer model, this method utilizes voltage feedforward term as a machine mathematical model. Its control block diagram is illustrated in Fig. 19, where blocks inside a dotted rectangle constitute a machine plant model. If d-axis feedforward voltage no longer matches the motor physical d-axis voltage, the current regulator compensates for the difference by outputting voltage $v_{d(\mathrm{PI})}$. This nonzero voltage is used to estimate $\Delta\theta$ through a gain term $\frac{-1}{\hat{\omega}\lambda_m}$. A PLL is then used to estimate rotor speed $\hat{\omega}$ and rotor position $\hat{\theta}$ from $\Delta\theta$. In Fig. 19, the red dashed line depicts disturbance rejection path through the estimated position $\hat{\theta}$, and the blue dashed line stands for disturbance rejection via estimated omega $\hat{\omega}$.

This method is based on *d-axis voltage* modeling error. The machine model inside voltage feedforward only covers the steady-state model. In Fig. 19, the dashed rectangle shows that this sensorless method can be treated as the filter form of an observer. The R_s block inside voltage feedforward can be moved inside the observer filter form so that the observer is a function of both the output voltage v_{dq}^* and sampled current i_{dq}. However, inductor transient voltage drop [② in (28)] term is not considered in this model. Meanwhile, $Q(s)$ filter in (20) and Fig. 9(b), being the symbol for the observer filter form, is not implemented in Fig. 19. This indicates that no corresponding observer IMO form can be found. A few comments are made here to characterize this method.

1) To track speed and position of an actual motor during fast acceleration or deceleration, a current command tracking error between d-axis reference current and feedback current is expected so that enough output voltage $v_{d(PI)}$ is available to correct estimated speed and position. This current tracking error degrades system performance for demanding applications.
2) On the other hand, any transient, initiated by current command change, injects disturbances into estimated speed and position.
3) Machine modeling error due to parameter inaccuracy causes additional output from the current PI regulator. This output drives the estimated speed and position away from its actual value. In short, the accuracy of the estimated speed and position is strongly modeling parameter dependent.

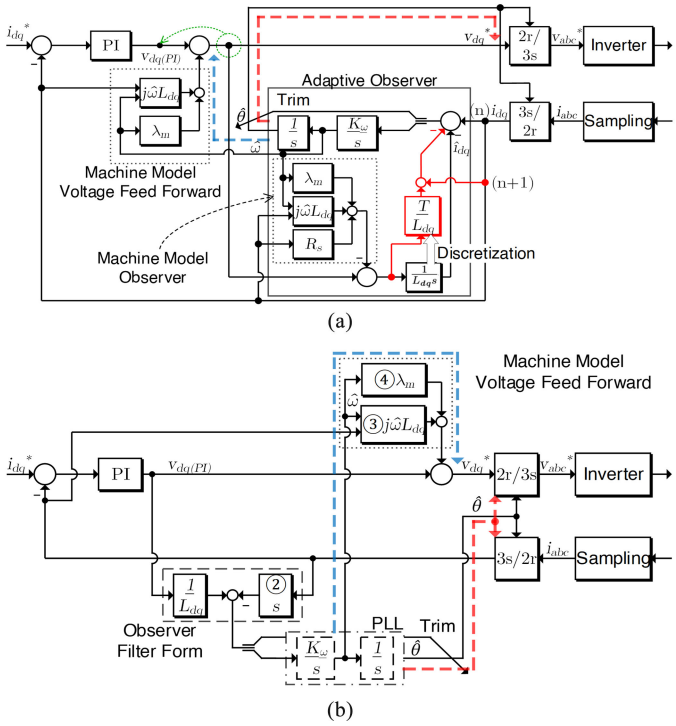

Fig. 20. Sensorless control using Matsui's method. (a) Matsui's method original version. (b) Matsui's method simplified version.

2) Matsui's Method: A SyncRF based "adaptive observer" is proposed in [56]–[62]. Fig. 20(a) shows the block diagram of this proposed method. Besides the steady-state machine model residing in the voltage feedforward term, a separate machine model

$$\begin{bmatrix} v_d \\ v_q \end{bmatrix} = \underbrace{R_s \begin{bmatrix} i_d \\ i_q \end{bmatrix}}_{①\text{resistor}} + \underbrace{\begin{bmatrix} pL_d & 0 \\ 0 & pL_q \end{bmatrix} \begin{bmatrix} i_d \\ i_q \end{bmatrix}}_{②\text{inductor}} + \underbrace{\begin{bmatrix} 0 & -\omega_r L_q \\ \omega_r L_d & 0 \end{bmatrix} \begin{bmatrix} i_d \\ i_q \end{bmatrix}}_{③\text{cross coupling}} + \underbrace{\begin{bmatrix} 0 \\ \omega_r \lambda_m \end{bmatrix}}_{④\text{emf}} \tag{28}$$

$$\begin{bmatrix} v_d \\ v_q \end{bmatrix} = \underbrace{R_s \begin{bmatrix} i_d \\ i_q \end{bmatrix}}_{①\text{resistor}} + \underbrace{pL_d \begin{bmatrix} i_d \\ i_q \end{bmatrix}}_{②\text{inductor}} + \underbrace{\begin{bmatrix} 0 & -\omega_r L_q \\ \omega_r L_q & 0 \end{bmatrix} \begin{bmatrix} i_d \\ i_q \end{bmatrix}}_{③\text{cross coupling}} + \underbrace{\begin{bmatrix} \omega_r \left(\lambda_m + (L_d - L_q) i_d\right) + (L_q - L_d) \dot{i}_q \end{bmatrix} \begin{bmatrix} 0 \\ 1 \end{bmatrix}}_{④\text{extended emf}} \tag{29}$$

$$\begin{bmatrix} v_d \\ v_q \end{bmatrix} = \underbrace{R_s \begin{bmatrix} i_d \\ i_q \end{bmatrix}}_{①\text{resistor}} + \underbrace{pL_q \begin{bmatrix} i_d \\ i_q \end{bmatrix}}_{②\text{inductor}} + \underbrace{\begin{bmatrix} 0 & -\omega_r L_q \\ \omega_r L_q & 0 \end{bmatrix} \begin{bmatrix} i_d \\ i_q \end{bmatrix}}_{③\text{cross coupling}} + \underbrace{\omega_r \left(\lambda_m + (L_d - L_q) i_d\right) \begin{bmatrix} 0 \\ 1 \end{bmatrix}}_{④\text{active flux}}. \tag{30}$$

is created inside the observer. Since both models use the same machine parameters and sampled current feedback, they can be consolidated by moving the observer voltage input junction from *dq* axes final output voltage v^*_{dq} to current regulator output voltage $v_{dq(\mathrm{PI})}$ (denoted by green dotted line with arrow). By doing this, the steady-state machine model inside the observer can be removed. In Fig. 20(a), the motor stator inductance, modeled as $\frac{1}{L_{dq}s}$ in continuous domain, is discretized using blocks highlighted in solid red lines as an approximation. This is different from standard discretization rules, such as the forward Euler method, backward Euler method, and trapezoidal method. As a result, the control block diagram in Fig. 20(a) [56]–[62] can be simplified to that in Fig. 20(b). Now, comparing Fig. 20(b) with Fig. 19, they share a few common features. Here, three major differences are listed in the following.

1) The estimated speed and position for Matsui's method are originated from *q-axis voltage* modeling error. D-axis voltage error is only used to trim the estimated angle.
2) Pure integrator is used to derive estimated speed instead of a PI regulator in Fig. 19.
3) Fig. 20(b) considers a machine transient model by applying derivative to feedback current (②). As mentioned in Section III-C2, the derivative operation is not preferable primarily due to the noise it creates. The actual implementation in Fig. 20(a) uses integration $\frac{1}{L_{dq}s}$ instead.

In Fig. 20(b), the rectangle with a dashed line shows the observer filter form. The inductance voltage drop [② in (28)] is now included but the resistor voltage drop [① in (28)] is not. Similar to Section VI-A1, $Q(s)$ filter is not applied in Fig. 20(b).

3) Morimoto's Method: The above two methods adopt observer filter form built upon the original machine *dq* axes model in (1) and (28). Alternatively, the model variant using extended-EMF voltage depicted in (5) and (29) can build an observer using its filter form [4], [63]. Fig. 21(a) plots the block diagram of this method. Both voltage feedforward and observer have their individual machine model. If these two models are combined together, Fig. 21(b) is derived. In Fig. 21(b), the extended-EMF voltage exists in the estimated extended back EMF voltage vector $[e_d\ e_q]^T$ rather than in voltage feedforward term. Although both *dq* extended-EMF voltages are used to derive angle error, this method can still be treated as *d-axis voltage error* in consideration of the approximation in (31). For Matsui's method in Fig. 20(b), since back EMF voltage is incorporated within voltage feedforward term, *q-axis voltage error* is used to derive the estimated speed and position

$$\tan^{-1}\left(\frac{e_d}{e_q}\right) \approx \tan^{-1}(e_d) \approx e_d \approx \Delta\theta. \tag{31}$$

Fig. 21(b) is treated as the observer filter form. The extended-EMF voltage [④ in (29)] appears as the estimated disturbance at the output of the observer. The LPF block $\frac{g}{s+g}$ operates as the $Q(s)$ filter.

4) Adaptive Observer Method: All the above methods in SyncRF adopt the filter form of an observer, while IMO form implementation of the observer has been reported in literature with different adaptive mechanisms [64]–[68]. Fig. 22 shows a typical example of the adaptive observer proposed in [66]–[68]. The word "Adaptive" is used in its name mainly attributed to the fact that the machine model, Luenberger gain, and adaptive gain could all or partially be adaptive to motor estimated speed. A few comments are made about this method.

1) The same back EMF voltage [④ in (28)] exists in both voltage feedforward term and observer. It can be combined and added to the final voltage command as shown in Fig. 22.
2) The machine model in voltage feedforward term and that in observer uses different current inputs. The feedforward term uses motor sampled current, while the observer uses motor estimated current. The source of the current signal

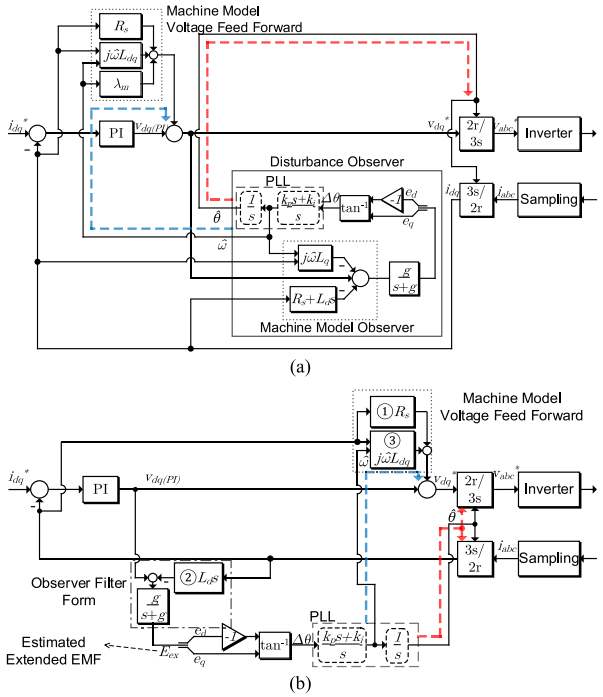

Fig. 21. Morimoto's extended-EMF observer method. (a) Original implementation. (b) Simplified implementation.

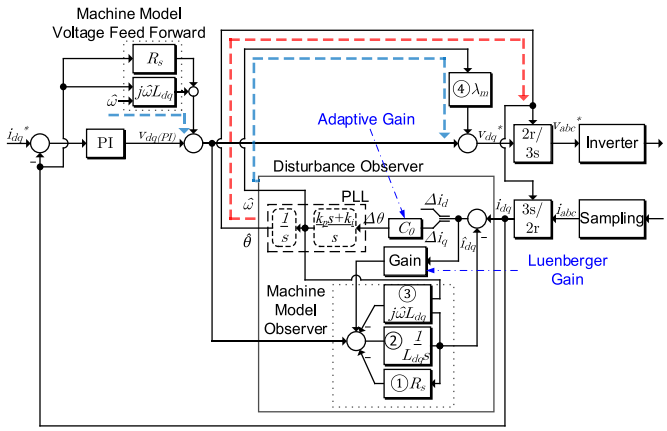

Fig. 22. Sensorless control using an adaptive observer.

TABLE III
CLASSIFICATION OF PUBLISHED LITERATURES

Literatures					
Z. Chen[3]	A1	B2	C2	D1	E4
Active Flux[2]	A1	B3	C1	D2	E1
SMO StatRF[14]–[16]	A1	B1	C2	D1	E2
SMO SyncRF[73]–[75]	A2	B1	C2	D1	E2
EKF StatRF[17], [18]	A1	B1	C2	D1	E3
EKF SyncRF[19]	A2	B1	C2	D2	E3
Adaptive Observer[64]–[68]	A2	B1	C2	D1	E4
N. Matsui[56]–[62]	A2	B1	C2	D1	N/A
S. Morimoto[4], [63]	A1	B2	C2	D1	E1
G. Foo[37]	A1	B3	C1	D1	E1
B. H. Bae[55]	A2	B1	C2	D2	N/A

can make a significant impact on the final sensorless control performance.

3) There are a few more gains inside the observer. The PLL gain, the Luenberger gain, and the adaptive gain. The tuning of these gains affects the overall system performance at different speeds and load conditions [67]. The Luenberger gain is supposed to only have proportional gain rather than PI gains for the best modeling error adaption.

5) Summary: A summary is made here about sensorless control in SyncRF.

1) Sensorless control in SyncRF calculates theta error $\Delta\theta$ based on the difference between the actual machine plant and the embedded mathematical plant model. This error can be retrieved from either *d-axis voltage error* or *q-axis voltage error*. If only *d-axis voltage error* is used, a sensorless algorithm itself does not require motor PM back EMF coefficient.
2) All above sensorless methods in SyncRF use different adaptation mechanisms and different gains to approach $\Delta\theta$. This $\Delta\theta$ derives the final speed and position through a PLL. Although steady-state performance difference is less obvious, these gains and adaption mechanisms could determine the dynamics of sensorless systems substantially (sensorless speed loop bandwidth for example).
3) Depending on where the command voltage is brought into the observer, the machine model in voltage feedforward term and that inside observer could be consolidated, especially for observer implemented using filter form.

B. Observer Filter Form Versus IMO Form for Sensorless Control in SyncRF

1) Transfer Function Block Diagram: Section IV-A demonstrates that observer IMO form and filter form are the same mathematical equation in two different representations. A simple inductor model $P(s) = \frac{1}{Ls}$ and proportional observer gain $C(s) = k$ are used as an example. However, the actual machine dq axes plant model uses complex vector representation [69], [70] as

$$P(s) = \frac{i_{dq}}{v_{dq} - \omega\lambda_m} = \frac{1}{L_{dq}s + R_s + j\omega L_{dq}}. \quad (32)$$

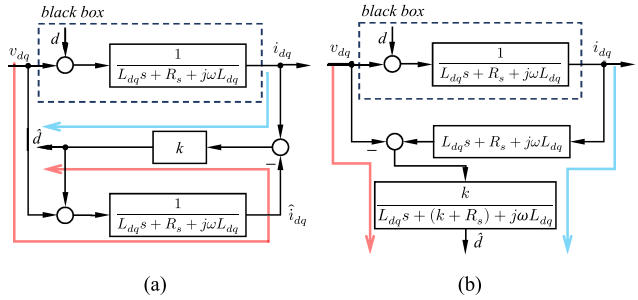

Fig. 23. Machine observer in SyncRF. (a) IMO form. (b) Filter form.

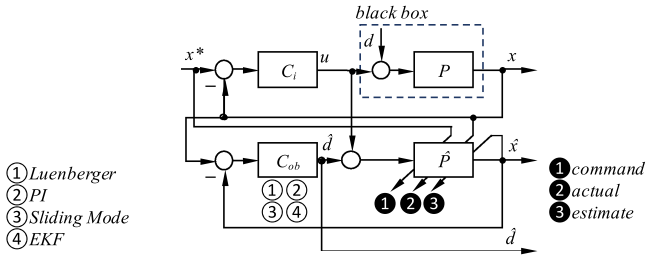

Fig. 24. Observer with different types of regulators and current sources for a machine model.

If Luenberger proportional gain $C(s) = k$ is still applied, the $Q(s)$ filter in (20) can be expressed as

$$Q(s) = \frac{k}{L_{dq}s + (k + R_s) + j\omega L_{dq}}. \quad (33)$$

By adopting the similar observer filter form concept explained in (23) and Fig. 9(b), the observer filter form in Fig. 23(b) has to use $Q(s)$ filter in the complex conjugate form to achieve the equivalent mathematical transfer function. However, these proposed sensorless control implementations elaborated in Section IV-A1, Section IV-A2, and Section IV-A3 either do not use $Q(s)$ filter or use a very simple first-order linear LPF. Therefore, the IMO form based adaptive observer in Section IV-A4 is always different mathematically from the ones in Section IV-A1, Section IV-A2, and Section IV-A3, which are implemented in observer filter form.

2) Current Being Used in the Plant Model: Comparative study between various methods using transfer functions offers an intuitive way of understanding the difference between observer IMO form and filter form in SyncRF. An alternative way of doing a comparison is to examine the source of current for machine modeling. These different sensorless methods reviewed in Section VI-A show that the observer filter form uses feedback current i_{fdbk} and observer IMO form uses estimate current i_{est} in their respective machine models. Fig. 24 shows there are three possible current sources: command current i_{cmd} (❶), feedback current i_{fdbk} (❷), and estimated current i_{est} (❸). To decide the right current source, the adaptation to parameter errors for each different current source is investigated in the following.

Back EMF based sensorless angle estimation accuracy is susceptible to machine modeling error since it is still a model-based approach. For an electric circuit or a magnetic circuit, the current

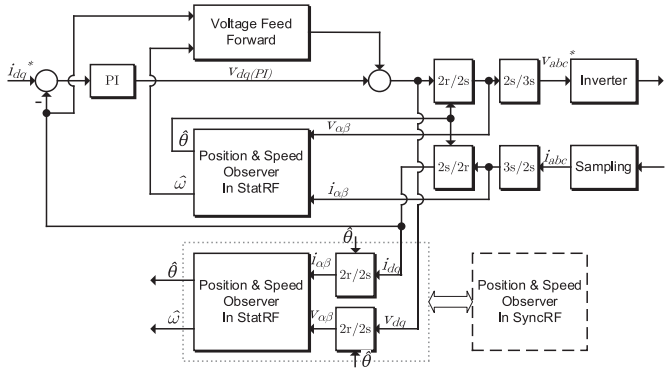

Fig. 25. Connection between sensorless control in StatRF and in SyncRF.

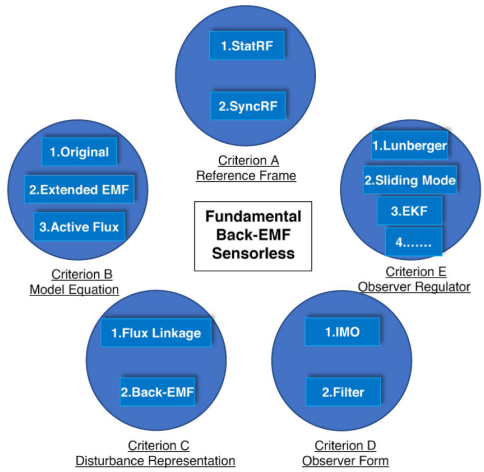

Fig. 26. Sensorless control classification based on different criteria.

or magnetic flux always tries to find the least resistive path. Applying the same theory for sensorless control, the parameter error accumulates at the "lowest equivalent resistance position" within the control loop. For an observer in filter form, this least resistance position happens to be at the estimated position since the *dq* current loop integrators do not allow constant input error. However, for an observer in IMO form, Luenberger gain K_p is only a proportional gain rather than a PI gain. The estimated current i_{est} can always be different from feedback current i_{fdbk} even at a steady state. Thus, the parameter error splits and manifests itself as both observed state error and estimated angle error. The adaptive gain C_0 in Fig. 22 adjusts the error distribution between estimate current error and estimate position error. In short, observer IMO form in Section VI-A4 presents less position estimation error in case of machine parameter error.

Fig. 24 also shows observer regulator C_{ob} can adopt all different types of regulators that have been mentioned in Section V.C.2) in StatRF. However, adopting a linear Luenberger gain by C_{ob} can handle a dc signal reasonably well in SyncRF.

VII. Summary

A. Connection Between Sensorless Control in StatRF and in SyncRF

Section V reviewed sensorless controls in StatRF and Section VI compared different sensorless algorithms in SyncRF. Fig. 25 shows a diagram that can explain the sensorless control relationship between StatRF and SyncRF.

Where

3s/2s Clark transformation.

2s/2r Park transformation.

2r/2s inverse Park transformation.

2s/3s inverse Clark transformation.

In Fig. 25, the inputs to the observer in StatRF are $\alpha\beta$ axes voltage $v_{\alpha\beta}$ and current $i_{\alpha\beta}$. With two inverse park transformation blocks $2r/2s$ incorporated, the inputs become *dq* axes voltage v_{dq} and current i_{dq}, although sensorless algorithm is still implemented in StatRF. If the two $2r/2s$ blocks in the dotted rectangle block in Fig. 25 are merged into the StatRF observer. The StatRF observer, in fact, becomes a SynRF observer considering all its input voltage and current are variables in *dq* axes. In short, an observer in StatRF can be converted to an observer in SyncRF. The reverse operation should hold as well. If a sensorless observer is built-in SyncRF, it can be converted into StatRF using two park transformation blocks $2s/2r$.

This mutual conversion between implementations in StatRF and SyncRF has been demonstrated by the design of a current regulator [53], [54], where a linear regulator in SyncRF, either a P or a PI, can be converted to a resonant regulator in StatRF with its resonant frequency at motor operating frequency. The detailed conversion steps are not included in this article.

B. Back EMF Based Sensorless Methods Classification

Back EMF based sensorless control has been reviewed in this article from different perspectives. The classification of various methods is critical for understanding the difference between different methods and for future sensorless technology development. For example, research in [2] and [28]–[36] interpreted difference methods as either open-loop calculation method or closed-loop observer method. While, research in [71] classified sensorless methods into back EMF estimation based methods and state observers and EKF method.

In this section, a preferred classification is summarized in the following based on five criteria.

Criterion A: Reference frames that sensorless control is implemented such as StatRF or SyncRF.

Criterion B: Machine modeling equations such as original equation, extended EMF, or active flux.

Criterion C: Disturbance representation such as flux linkage or back EMF voltage.

Criterion D: Forms of observers such as the IMO form or the filter form.

Criterion E: Form of observer regulators such as Luenberger, sliding mode, or EKF.

Fig. 26 shows five categories highlighted with circles. Inside each circle, rectangle blocks represent different options in the category. As a result, these methods published in literature can be classified using the above five categories. Table III shows the classification of existing literature in terms of the proposed five criteria.

VIII. Conclusion

This article reviewed the common practice of doing sensorless control for a synchronous machine based on back EMF voltage with a focus on unveiling fundamental connections between different methods. This article categorized various methods based on several criteria. The main contributions of this article are summarized as follows.

1) A unified systematic overview of synchronous machine flux vector control with and without a position sensor was performed. To properly analyze system dynamics for different sensorless algorithms, a sensorless algorithm itself, current regulator, and machine plant model were evaluated at equal weight as a complete system.
2) The machine mathematical model in its original representation as well as two variants was summarized. These variants offer a convenient way of doing sensorless control in StatRF.
3) The basic theory of an observer was revisited. The IMO form and filter form describe the same observer model in two different ways. The conventional named "open-loop sensorless calculation method" can be treated as the filter form of the observer.
4) For sensorless in StatRF, the flux linkage calculation-based method and the back EMF observer voltage-based method were verified to be the same method in two representations. However, filter phase deviation associated with disturbance observer is the key issue for sensorless control in StatRF.
5) The typical sensorless control methods in SyncRF were reviewed. The fundamentals behind different methods in association with observer filter form and IMO form were explored. The observer IMO form uses estimated current, which provides a cushion for modeling error and system transients.
6) A summary is given to classify sensorless control methods in terms of five listed criteria.

Acknowledgment

The author would like to express his sincere gratitude to Robert Miklosovic for his instruction and heuristic discussion of classical control theory and its application to servo motion control systems over the years. The author would also like to thank Ahmed Sayed Ahmed and Jacob Lamb for proofreading the manuscript and offering very constructive advice.

References

[1] D. Nishijima and T. Morohoshi, "The sensorless servo "FR-E720EX & MM-GKR series"," *Mitsubishi Electr. Adv.*, vol. 150, 2015, Art. no. 1.
[2] I. Boldea, M. C. Paicu, and G. D. Andreescu, "Active flux concept for motion-sensorless unified AC drives," *IEEE Trans. Power Electron.*, vol. 23, no. 5, pp. 2612–2618, Sep. 2008.
[3] Z. Chen, M. Tomita, S. Doki, and S. Okuma, "An extended electromotive force model for sensorless control of interior permanent-magnet synchronous motors," *IEEE Trans. Ind. Electron.*, vol. 50, no. 2, pp. 288–295, Apr. 2003.
[4] S. Morimoto, K. Kawamoto, M. Sanada, and Y. Takeda, "Sensorless control strategy for salient-pole PMSM based on extended EMF in rotating reference frame," *IEEE Trans. Ind. Appl.*, vol. 38, no. 4, pp. 1054–1061, Jul./Aug. 2002.
[5] J. X. Shen and S. Iwasaki, "Sensorless control of ultra high-speed PM brushless motor using PLL and third harmonic back EMF," *IEEE Trans. Ind. Electron.*, vol. 53, no. 2, pp. 421–428, Apr. 2006.
[6] J. X. Shen, Z. Q. Zhu, and D. Howe, "Sensorless flux-weakening control of permanent-magnet brushless machines using third harmonic back EMF," *IEEE Trans. Ind. Appl.*, vol. 40, no. 6, pp. 1629–1636, Nov. 2004.
[7] M. Pacas, "Sensorless drives in industrial applications," *IEEE Ind. Electron. Mag.*, vol. 5, no. 2, pp. 16–23, Jun. 2011.
[8] J. Holtz, "Sensorless position control of induction motors. an emerging technology," *IEEE Trans. Ind. Electron.*, vol. 45, no. 6, pp. 840–851, Dec. 1998.
[9] M. W. Degner and R. D. Lorenz, "Position estimation in induction machines utilizing rotor bar slot harmonies and carrier-frequency signal injection," *IEEE Trans. Ind. Appl.*, vol. 36, no. 3, pp. 736–742, May-Jun. 2000.
[10] J. Cilia, G. M. Asher, K. J. Bradley, and M. Sumner, "Sensorless position detection for vector-controlled induction motor drives using an asymmetric outer-section cage," *IEEE Trans. Ind. Appl.*, vol. 33, no. 5, pp. 1162–1169, Sep. 1997.
[11] J. H. Jang, S. K. Sul, J. I. Ha, K. Ide, and M. Sawamura, "Sensorless drive of surface-mounted permanent-magnet motor by high-frequency signal injection based on magnetic saliency," *IEEE Trans. Ind. Appl.*, vol. 39, no. 4, pp. 1031–1039, Jul. 2003.
[12] J. I. Ha and S. K. Sul, "Sensorless field orientation control of an induction machine by high-frequency signal injection," *IEEE Trans. Ind. Appl.*, vol. 35, no. 1, pp. 45–51, Jan./Feb. 1999.
[13] Y. D. Yoon, S. K. Sul, S. Morimoto, and K. Ide, "High-bandwidth sensorless algorithm for AC machines based on square-wave-type voltage injection," *IEEE Trans. Ind. Appl.*, vol. 47, no. 3, pp. 1361–1370, May 2011.
[14] S. Chi, Z. Zhang, and L. Xu, "Sliding-mode sensorless control of direct-drive PM synchronous motors for washing machine applications," *IEEE Trans. Ind. Appl.*, vol. 45, no. 2, pp. 582–590, Mar./Apr. 2009.
[15] Z. Yan and V. Utkin, "Sliding mode observers for electric machines—An overview," in *Proc. 28th Annu. Conf. Ind. Electron. Soc.*, 2002, vol. 3, pp. 1842–1847.
[16] G. Wang, R. Yang, and D. Xu, "DSP-based control of sensorless IPMSM drives for wide-speed-range operation," *IEEE Trans. Ind. Electron.*, vol. 60, no. 2, pp. 720–727, Feb. 2013.
[17] S. Bolognani, R. Oboe, and M. Zigliotto, "DSP-based extended Kalman filter estimation of speed and rotor position of a PM synchronous motor," in *Proc. 20th Annu. Conf. IEEE Ind. Electron.*, 1994, vol. 3, pp. 2097–2102.
[18] S. Bolognani, L. Tubiana, and M. Zigliotto, "Extended Kalman filter tuning in sensorless PMSM drives," *IEEE Trans. Ind. Appl.*, vol. 39, no. 6, pp. 1741–1747, Nov./Dec. 2003.
[19] S. Bolognani, L. Tubiana, and M. Zigliotto, "EKF-based sensorless IPM synchronous motor drive for flux-weakening applications," *IEEE Trans. Ind. Appl.*, vol. 39, no. 3, pp. 768–775, May 2002.
[20] D. Liang, J. Li, and R. Qu, "Sensorless control of permanent magnet synchronous machine based on second-order sliding-mode observer with online resistance estimation," *IEEE Trans. Ind. Appl.*, vol. 53, no. 4, pp. 3672–3682, Jul./Aug. 2017.
[21] B. Du, S. Wu, S. Han, and S. Cui, "Application of linear active disturbance rejection controller for sensorless control of internal permanent-magnet synchronous motor," *IEEE Trans. Ind. Electron.*, vol. 63, no. 5, pp. 3019–3027, May 2016.
[22] X. Wu *et al.*, "Enhanced position sensorless control using bilinear recursive least squares adaptive filter for interior permanent magnet synchronous motor," *IEEE Trans. Power Electron.*, vol. 35, no. 1, pp. 681–698, Jan. 2020.
[23] L. Sheng, W. Li, Y. Wang, M. Fan, and X. Yang, "Sensorless control of a shearer short-range cutting interior permanent magnet synchronous motor based on a new sliding mode observer," *IEEE Access*, vol. 5, pp. 18439–18450, 2017.
[24] Y. Fan, L. Zhang, J. Huang, and X. Han, "Design, analysis, and sensorless control of a self-decelerating permanent-magnet in-wheel motor," *IEEE Trans. Ind. Electron.*, vol. 61, no. 10, pp. 5788–5797, Oct. 2014.
[25] J. J. Ren, Y. C. Liu, N. Wang, and S. Y. Liu, "Sensorless control of ship propulsion interior permanent magnet synchronous motor based on a new sliding mode observer," *ISA Trans.*, vol. 54, no. 2, pp. 15–26, 2015.
[26] K. Urbanski and D. Janiszewski, "Sensorless control of the permanent magnet synchronous motor," *Sensors*, vol. 19, no. 16, 2019, Art. no. 3546.
[27] J. Choi, K. Nam, A. A. Bobtsov, A. Pyrkin, and R. Ortega, "Robust adaptive sensorless control for permanent-magnet synchronous motors," *IEEE Trans. Power Electron.*, vol. 32, no. 5, pp. 3989–3997, May 2017.
[28] G. Wang, M. Valla, and J. Solsona, "Position sensorless permanent magnet synchronous machine drives—A review," *IEEE Trans. Ind. Electron.*, vol. 67, no. 7, pp. 5830–5842, Jul. 2020.

[29] G. Zhang, G. Wang, and D. Xu, "Saliency-based position sensorless control methods for PMSM drives-A review," *Chin. J. Elect. Eng.*, vol. 3, no. 2, pp. 14–23, 2019.
[30] S. Singh and A. N. Tiwari, "Various techniques of sensorless speed control of PMSM: A review," in *Proc. 2nd IEEE Int. Conf. Elect. Comput. Commun. Technol.*, 2017, pp. 1–6.
[31] Y. Zhao, C. Wei, Z. Zhang, and W. Qiao, "A review on position/speed sensorless control for permanent-magnet synchronous machine-based wind energy conversion systems," *IEEE J. Emerg. Sel. Topics Power Electron.*, vol. 1, no. 4, pp. 203–216, Dec. 2013.
[32] I. M. Alsofyani and N. R. N. Idris, "A review on sensorless techniques for sustainable reliablity and efficient variable frequency drives of induction motors," *Renewable Sustain. Energy Rev.*, vol. 24, pp. 111–121, 2013.
[33] R. Bojoi, M. Pastorelli, J. Bottomley, P. Giangrande, and C. Gerada, "Sensorless control of PM motor drives—A technology status review," in *Proc. IEEE Workshop Elect. Mach. Des., Control Diagnosis*, 2013, pp. 166–180.
[34] O. Benjak and D. Gerling, "Review of position estimation methods for IPMSM drives without a position sensor part II: Adaptive methods," in *Proc. 19th Int. Conf. Elect. Mach.*, 2010, pp. 1–6.
[35] T. Kim, H. W. Lee, and M. Ehsani, "Position sensorless brushless DC motor/generator drives: Review and future trends," *IET Elect. Power Appl.*, vol. 1, no. 4, pp. 557–564, 2007.
[36] P. P. Acarnley and J. F. Watson, "Review of position-sensorless operation of brushless permanent-magnet machines," *IEEE Trans. Ind. Electron.*, vol. 53, no. 2, pp. 352–362, Apr. 2006.
[37] G. Foo and M. F. Rahman, "Sensorless direct torque and flux-controlled IPM synchronous motor drive at very low speed without signal injection," *IEEE Trans. Ind. Electron.*, vol. 57, no. 1, pp. 395–403, Jan. 2010.
[38] J. Liu, T. A. Nondahl, P. B. Schmidt, S. Royak, and M. Harbaugh, "Rotor position estimation for synchronous machines based on equivalent EMF," *IEEE Trans. Ind. Appl.*, vol. 47, no. 3, pp. 1310–1318, May/Jun. 2011.
[39] N. Matsui, "Sensorless operation of brushless DC motor drives," in *Proc. 19th Annu. Conf. IEEE Ind. Electron.*, 1993, pp. 739–744.
[40] F. Parasiliti, R. Petrella, and M. Tursini, "Sensorless speed control of a PM synchronous motor by sliding mode observer," in *Proc. IEEE Int. Symp. Ind. Electron.*, 1997, pp. 1106–1111.
[41] S. Nakashima, Y. Inagaki, and I. Miki, "Sensorless initial rotor position estimation of surface permanent-magnet synchronous motor," *IEEE Trans. Ind. Appl.*, vol. 36, no. 6, pp. 1598–1603, Nov./Dec. 2000.
[42] M. Boussak, "Implementation and experimental investigation of sensorless speed control with initial rotor position estimation for interior permanent magnet synchronous motor drive," *IEEE Trans. Power Electron.*, vol. 20, no. 6, pp. 1413–1422, Nov. 2005.
[43] M. Tursini, R. Petrella, and F. Parasiliti, "Initial rotor position estimation method for PM motors," *IEEE Trans. Ind. Appl.*, vol. 39, no. 6, pp. 1630–1640, Nov./Dec. 2003.
[44] P. B. Schmidt, M. L. Gasperi, G. Ray, and A. H. Wijenayake, "Initial rotor angle detection of a nonsalient pole permanent magnet synchronous machine," in *Proc. Conf. Rec. IEEE Ind. Appl. Conf. 32nd IAS Annu. Meeting*, 1997, vol. 1, pp. 459–463.
[45] A. Radke and Z. Gao, "A survey of state and disturbance observers for practitioners," in *Proc. Amer. Control Conf.*, 2006, vol. 2006, pp. 5183–5188.
[46] Z. Gao, "Active disturbance rejection control: A paradigm shift in feedback control system design," in *Proc. Amer. Control Conf.*, 2006, pp. 2399–2405.
[47] R. Miklosovic, A. Radke, and Z. Gao, "Discrete implementation and generalization of the extended state observer," in *Proc. Amer. Control Conf.*, 2006, pp. 2209–2214.
[48] E. Schrijver and J. Van Dijk, "Disturbance observers for rigid mechanical systems: Equivalence, stability, and design," *J. Dyn. Syst., Meas., Control*, vol. 124, no. 4, pp. 539–548, 2002.
[49] G. Ellis, *Control System Design Guide: A Practical Guide*. San Diego, CA, USA: Elsevier, 2004.
[50] K. W. Lee and J. I. Ha, "Evaluation of back-EMF estimators for sensorless control of permanent magnet synchronous motors," *J. Power Electron.*, vol. 12, no. 4, pp. 604–614, 2012.
[51] D. Wang, K. Lu, and P. O. Rasmussen, "Improved closed-loop flux observer based sensorless control against system oscillation for synchronous reluctance machine drives," *IEEE Trans. Power Electron.*, vol. 34, no. 5, pp. 4593–4602, May 2019.
[52] D. G. Holmes, T. A. Lipo, B. P. McGrath, and W. Y. Kong, "Optimized design of stationary frame three phase AC current regulators," *IEEE Trans. Power Electron.*, vol. 24, no. 11, pp. 2417–2426, Nov. 2009.
[53] D. N. Zmood, D. G. Holmes, and G. H. Bode, "Frequency-domain analysis of three-phase linear current regulators," *IEEE Trans. Ind. Appl.*, vol. 37, no. 2, pp. 601–610, Mar./Apr. 2001.
[54] D. N. Zmood and D. G. Holmes, "Stationary frame current regulation of PWM inverters with zero steady-state error," *IEEE Trans. Power Electron.*, vol. 18, no. 3, pp. 814–822, May 2003.
[55] B. H. Bae, S. K. Sul, J. H. Kwon, and J. S. Byeon, "Implementation of sensorless vector control for super-high-speed PMSM of turbo-compressor," *IEEE Trans. Ind. Appl.*, vol. 39, no. 3, pp. 811–818, May/Jun. 2003.
[56] T. Takeshita, A. Usui, and N. Matsui, "Sensorless salient-pole PM synchronous motor drives in all speed ranges," *IEEJ Trans. Ind. Appl.*, vol. 120, no. 2, pp. 240–247, 2000.
[57] N. Matsui and H. Ohashi, "DSP-based adaptive control of a brushless motor," *IEEE Trans. Ind. Appl.*, vol. 28, no. 2, pp. 448–454, Mar./Apr. 1992.
[58] T. Takeshita and N. Matsui, "Sensorless control and initial position estimation," in *Proc. 4th IEEE Int. Workshop Adv. Motion Control*, 1996, vol. 1, pp. 18–23.
[59] R. Mizutani, T. Takeshita, and N. Matsui, "Current model-based sensorless drives of salient-pole PMSM at low speed and standstill," *IEEE Trans. Ind. Appl.*, vol. 34, no. 4, pp. 841–846, Jul./Aug. 1998.
[60] N. Matsui, "Sensorless PM brushless DC motor drives," *IEEE Trans. Ind. Electron.*, vol. 43, no. 2, pp. 300–308, Apr. 1996.
[61] K. Y. Cho, S. B. Yang, and C. H. Hong, "Sensorless control of a PM synchronous motor for direct drive washer without rotor position sensors," in *Proc. Inst. Elect. Eng.—Elect. Power Appl.*, 2004, vol. 151, no. 1, pp. 61–69.
[62] T. Takeshita and N. Matsui, "Sensorless control and initial position estimation of salient-pole brushless DC motor," in *Proc. Int. Workshop Adv. Motion Control*, 1996, vol. 1, pp. 18–23.
[63] S. Morimoto, M. Sanada, and Y. Takeda, "Mechanical sensorless drives of IPMSM with online parameter identification," *IEEE Trans. Ind. Appl.*, vol. 42, no. 5, pp. 1241–1248, Sep./Oct. 2006.
[64] M.-H. Park and H.-H. Lee, "Sensorless vector control of PMSM using adaptive identification," in *Proc. 15th Annu. Conf. IEEE Ind. Electron. Soc.*, 1989, pp. 209–214.
[65] X. Xiao, Y. Li, M. Zhang, and Y. Liang, "A sensorless control based on MRAS method in interior permanent-magnet machine drive," in *Proc. Int. Conf. Power Electron. Drive Syst.*, 2005, vol. 1, pp. 734–738.
[66] A. Piippo, M. Hinkkanen, and J. Luomi, "Sensorless control of PMSM drives using a combination of voltage model and HF signal injection," in *Proc. Conf. Rec. IEEE IAS Annu. Meeting*, 2004, pp. 964–970.
[67] A. Piippo, M. Hinkkanen, and J. Luomi, "Analysis of an adaptive observer for sensorless control of interior permanent magnet synchronous motors," *IEEE Trans. Ind. Electron.*, vol. 55, no. 2, pp. 570–576, Aug. 2008.
[68] A. Piippo, M. Hinkkanen, and J. Luomi, "Adaptation of motor parameters in sensorless PMSM drives," *IEEE Trans. Ind. Appl.*, vol. 45, no. 1, pp. 203–212, Jan./Feb. 2009.
[69] F. Briz, M. W. Degner, and R. D. Lorenz, "Analysis and design of current regulators using complex vectors," *IEEE Trans. Ind. Appl.*, vol. 36, no. 3, pp. 817–825, May/Jun. 2000.
[70] F. B. Del Blanco, M. W. Degner, and R. D. Lorenz, "Dynamic analysis of current regulators for ac motors using complex vectors," *IEEE Trans. Ind. Appl.*, vol. 35, no. 6, pp. 1424–1432, Nov./Dec. 1999.
[71] B. Nahid-Mobarakeh, F. Meibody-Tabar, and F. M. Sargos, "Mechanical sensorless control of PMSM with online estimation of stator resistance," *IEEE Trans. Ind. Appl.*, vol. 40, no. 2, pp. 457–471, Mar./Apr. 2004.
[72] N. Matsui, "Sensorless PM brushless DC motor drives," *IEEE Trans. Ind. Electron.*, vol. 43, no. 2, pp. 300–308, Apr. 1996.
[73] Z. Xu and M. F. Rahman, "An adaptive sliding stator flux observer for a direct-torque-controlled IPM synchronous motor drive," *IEEE Trans. Ind. Electron.*, vol. 54, no. 5, pp. 2398–2406, Oct. 2007.
[74] Z. Xu and M. F. Rahman, "Direct torque and flux regulation of an IPM synchronous motor drive using variable structure control approach," *IEEE Trans. Power Electron.*, vol. 22, no. 6, pp. 2487–2498, Nov. 2007.
[75] G. Foo and M. F. Rahman, "Sensorless sliding-mode MTPA control of an IPM synchronous motor drive using a sliding-mode observer and HF signal injection," *IEEE Trans. Ind. Electron.*, vol. 57, no. 4, pp. 1270–1278, Apr. 2010.
[76] A. Piippo, M. Hinkkanen, and J. Luomi, "Analysis of an adaptive observer for sensorless control of interior permanent magnet synchronous motors," *IEEE Trans. Ind. Electron.*, vol. 55, no. 2, pp. 570–576, Feb. 2008.